

Article

Not peer-reviewed version

---

# Effects of Ignition Delay on Flame Behavior and Local Thermal Response of Non-Uniform Hydrogen-Blended Natural Gas Clouds Formed by Soil Seepage

---

Wenxin Guo , [Shaohua Dong](#) <sup>\*</sup> , [Haotian Wei](#) <sup>\*</sup> , Jiamei Li

Posted Date: 5 May 2026

doi: 10.20944/preprints202605.0171.v1

Keywords: hydrogen-blended natural gas; soil seepage; ignition delay; non-uniform combustion cloud; flame behavior; local thermal response



Preprints.org is a free multidisciplinary platform providing preprint service that is dedicated to making early versions of research outputs permanently available and citable. Preprints posted at Preprints.org appear in Web of Science, Crossref, Google Scholar, Scilit, Europe PMC, OpenAlex.

Copyright: This open access article is published under a [Creative Commons CC BY 4.0 license](#), which permit the free download, distribution, and reuse, provided that the author and preprint are cited in any reuse.

Disclaimer/Publisher's Note: The statements, opinions, and data contained in all publications are solely those of the individual author(s) and contributor(s) and not of MDPI and/or the editor(s). MDPI and/or the editor(s) disclaim responsibility for any injury to people or property resulting from any ideas, methods, instructions, or products referred to in the content.

Article

# Effects of Ignition Delay on Flame Behavior and Local Thermal Response of Non-Uniform Hydrogen-Blended Natural Gas Clouds Formed by Soil Seepage

Wenxin Guo <sup>1</sup>, Shaohua Dong <sup>1,\*</sup>, Haotian Wei <sup>2,\*</sup> and Jiamei Li <sup>1</sup>

<sup>1</sup> College of Safety and Ocean Engineering, China University of Petroleum (Beijing), Beijing, 102249, PR China

<sup>2</sup> College of Mechanical and Transportation Engineering, China University of Petroleum (Beijing), Beijing, 102249, PR China

\* Correspondence: shdong@cup.edu.cn (S.D.); weihaotian@cup.edu.cn (H.W.); Tel: +86-10-15210718180

## Abstract

After leakage from buried hydrogen-blended natural gas pipelines, gas may seep through soil into enclosed spaces and form buoyancy-driven non-uniform combustible clouds. The effect of ignition delay on such clouds remains insufficiently understood, especially regarding the relationship between visible flame behavior and local thermal response. In this study, 44 soil-seepage combustion experiments were conducted in a 1.5 m × 1.5 m × 1.5 m enclosure. Methane and hydrogen concentrations at three heights, flame evolution, and transient temperatures were measured using gas sensors, high-speed imaging, and thermocouples. The ignition delay ranged from 27 s to 5429 s, with hydrogen blending ratios of 10–30 vol% and ignition positions at the floor, middle, and ceiling. The results show that longer ignition delays generally weakened visible flame luminosity and propagation extent. However, the peak temperature measured at the central thermocouple did not decrease accordingly. For the long-delay subset with  $t_a > 307$  s, the central peak temperature increased with ignition delay, with  $R^2 = 0.74$ . Concentration measurements indicate that preferential hydrogen migration and slower methane redistribution continuously reconfigured the local flammability state before ignition. These findings suggest that, in enclosed soil-seepage HBNG scenarios, prolonged ignition delay may weaken visible flames but does not necessarily reduce local thermal exposure.

**Keywords:** hydrogen-blended natural gas; soil seepage; ignition delay; non-uniform combustion cloud; flame behavior; local thermal response

## 1. Introduction

Blending hydrogen into natural gas pipeline networks is regarded as a practical transitional approach for reducing the carbon intensity of pipeline-transported fuels [1–3]. It supports the low carbon transition of energy systems by adjusting the hydrogen and carbon composition of the gas supplied through pipeline networks [4,5]. However, hydrogen has a low molecular weight, a high diffusion coefficient, wide flammability limits and a low ignition energy. These properties make the leakage, diffusion and ignition risks of hydrogen-blended natural gas different from those of conventional natural gas [6–8]. After leakage from a buried hydrogen-blended natural gas (HBNG) pipeline, the released gas may seep upward through soil pores and enter overlying enclosed underground spaces such as utility tunnels. Under the combined effects of buoyancy and molecular diffusion, a non-uniform flammable cloud with a vertical concentration gradient can form [9–12].

Previous studies have advanced the understanding of HBNG safety by examining leakage diffusion, ventilation, premixed combustion, explosion characteristics and risk assessment under different conditions [13–20]. Key factors investigated in these studies include hydrogen blending

ratio(HBR), ignition position, initial fuel distribution, obstacles, ventilation conditions and enclosure configuration. These studies have established important knowledge of HBNG leakage and combustion behavior. However, these studies do not fully represent buried leakage scenarios in which the released gas migrates through soil, accumulates in an enclosed space, and continuously undergoes concentration redistribution before ignition.

In a typical buried HBNG pipeline leakage accident, a time interval usually exists between leakage cessation and ignition by an external source. This interval is defined in this paper as the ignition delay time. After leakage stops, the flow field gradually changes from momentum induced residual turbulence to buoyancy dominated motion. Light components continue to migrate under buoyancy, while the cloud boundary and local flammable zones continue to evolve. The ignition delay time affects the local composition distribution at the moment of ignition and may therefore influence flame development and local thermal response. Yang et al.[21] investigated the effect of millisecond scale diffusion time on pure hydrogen leakage explosion in a small pipe with both ends open and identified 800 ms as the critical time for the transition from turbulence dominated to buoyancy dominated behavior. However, the fuel type, boundary conditions, geometric scale, time scale and leakage pathway in their study differ fundamentally from those in HBNG leakage through soil into an enclosed space.

In this study, a buried-pipeline soil-seepage experimental platform was used to investigate the effect of ignition delay on the flame behavior and local thermal response of non-uniform HBNG clouds. A total of 44 experiments were conducted with ignition delays of 27–5429 s, HBRs of 10–30 vol%, and ignition positions at the floor, middle, and ceiling. By combining flame imaging, vertical concentration measurements, and transient temperature acquisition, this study reveals how post-leakage redistribution of  $\text{CH}_4$  and  $\text{H}_2$  affects visible flame development and local thermal exposure. The results provide experimental evidence for assessing ignition and thermal hazards after buried HBNG pipeline leakage.

## 2. Experimental Methods

### 2.1. Experimental Setup

The HBNG soil leakage combustion experimental platform is shown in Figure 1. The system consisted of an enclosed space simulator, a soil leakage unit, a high speed imaging system, a temperature acquisition system and an ignition system.

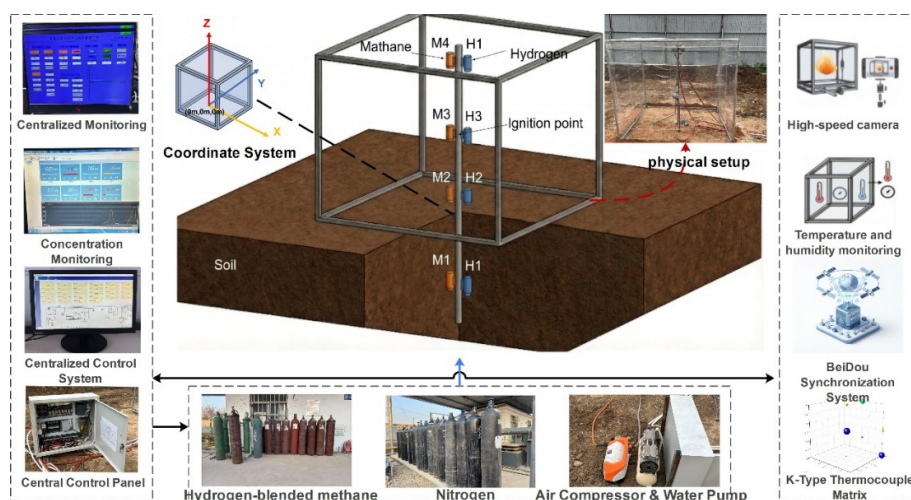


Figure 1. Experimental platform.

The enclosed space simulator was a metal frame structure with dimensions of 1500 mm × 1500 mm × 1500 mm. The enclosure was fully covered with a 0.22 mm transparent polyethylene (PE) film. All edges and joints were sealed before each test, and no ventilation opening was present during leakage, ignition delay, or pre-ignition stages. Minor leakage through film joints could not be completely excluded and is considered as an experimental uncertainty. The enclosure had no designed ventilation opening and was treated as a quasi-closed space during leakage, ignition delay, and the pre-ignition stage. In cases where the PE film failed, it first inflated and then ruptured after ignition, indicating that rupture was caused by combustion-induced pressure rise rather than pre-ignition leakage. An 800 mm deep soil pit was excavated beneath the enclosed space. The in-situ soil was replaced with medium grained washed sand to simulate the upward seepage of gas through a homogeneous porous medium after leakage from a buried pipeline.

Flame images were recorded by a high-speed camera at 240 fps. Flame morphology was evaluated qualitatively from high-speed images. The observed flame luminosity and visible propagation extent were used to describe the apparent visible-flame development, rather than to quantify the total combustion intensity.

Temperature was measured by seven type K thermocouples with 0.5 mm diameter exposed junctions. The sampling frequency was 1000 Hz, and the response time constant was approximately 0.05 s. The detailed arrangement of the thermocouples is shown in Figure 2 and Table 1. The main analysis in this study was based on K1, K2 and K3 along the central axis to characterize the vertical thermal response. K2 was located at the geometric center and was used as the representative point for evaluating the local point-measured thermal response near the center of the enclosure. The other thermocouples were used to assist in evaluating the spatial temperature distribution. The measured temperature represents the local gas-phase thermal response at the thermocouple junction. Because of heat losses, finite thermocouple response, and possible displacement between the flame front and the thermocouple junction, the measured peak temperature should be interpreted as a local thermal exposure indicator. It should not be interpreted as the flame temperature or the adiabatic combustion temperature of the HBNG–air mixture.

**Table 1.** Coordinates of K-type thermocouples.

Measurement point	X	Y	Z
K1	0 mm	0 mm	0 mm
K2	0 mm	0 mm	750 mm
K3	0 mm	0 mm	1500 mm
K4	750 mm	750 mm	0 mm
K5	750 mm	750 mm	750 mm
K6	0 mm	750 mm	1500 mm
K7	0 mm	750 mm	400 mm

Note. Coordinates are given in the order of x, y and z, where z represents the vertical height.

The ignition system used an electric spark igniter with three adjustable power settings. For each test, the discharge power and ignition duration were recorded, and the nominal electrical ignition energy was calculated as  $E=P \times t$ . The calculated ignition energy ranged from 160 mJ to 1600 mJ. This value represents the electrical input energy of the ignition system rather than the energy effectively deposited into the combustible mixture. Although ignition energy was recorded for each test, it was not independently varied as a controlled factor in this study and was therefore used only to document the ignition condition. The igniter was placed at the floor, middle, and ceiling positions, corresponding to approximate heights of 0 mm, 750 mm, and 1500 mm.

Methane and hydrogen concentrations at the bottom, middle, and top of the central axis were measured using gas sensors. The methane sensor had a measurement range of 0–100 vol%, whereas the hydrogen sensor had a measurement range of 0–4 vol%, with a resolution of 0.01 vol%. Before the experiments, the sensor calibration, response time, sampling-line delay, and potential cross-

sensitivity of the H<sub>2</sub> sensor to CH<sub>4</sub> were evaluated. Because the upper range of the H<sub>2</sub> sensor was close to the lower flammability limit of pure hydrogen in air, H<sub>2</sub> readings approaching 4 vol% were checked for possible saturation, and only unsaturated data were used for local flammability analysis. During the leakage stage, the gas supply was monitored and regulated to achieve the prescribed HBNG release volume for each experimental case.

The soil layer was filled with dry medium-grained washed sand. Because the experiments were conducted as outdoor field-scale soil-seepage tests, small variations in soil packing density, ambient conditions, and local seepage pathways were unavoidable. Therefore, exact repetition of each operating condition was difficult, and the analysis focused on overall trends across 44 valid experimental cases rather than on averaged repeated measurements under identical conditions.



**Figure 2.** Arrangement of thermocouples along the central axis.

## 2.2. Experimental Procedure and Test Conditions

The test gases were HBNG mixtures with HBRs of 10 vol%, 20 vol% and 30 vol%. The gas was injected into the bottom of the soil layer through a mass flow controller, then seeped upward and accumulated inside the enclosed space. The ignition delay time, denoted as  $t_a$ , was defined as the time interval between leakage cessation and ignition. During this stage, the flammable cloud evolved and restructured freely under the combined effects of residual momentum, buoyancy and molecular diffusion.

Table 2 summarizes the distribution of the 44 valid experimental cases in terms of ignition-delay range, global equivalence ratio, HBR, and ignition position. The ignition delay time  $t_a$  ranged from 27 s to 5429 s. Owing to fluctuations in the field soil-seepage and gas-accumulation processes, the global equivalence ratio  $\phi$  varied among the test conditions, ranging from 0.36 to 2.06. Therefore, this study did not rely on deterministic comparison of individual cases under nominally identical conditions. Instead, it examined trend-based evidence across the 44 valid cases to evaluate how the ignition-delay period was associated with flame behavior and local thermal-response characteristics. For each experiment, the peak temperature  $T_{\max}$  and the time to peak temperature  $t_{\max}$  were extracted from K2, which was used as the representative central measurement point.

**Table 2.** Summary of experimental conditions grouped by ignition delay time.

Stage	$t_d$ Range (s)	Cases	$\varphi$ Range	HBR(vol%)	Ignition position
I	<60	17	0.71–2.06	10/20/30	floor / middle / ceiling
II	60–300	14	0.48–1.72	10/20/30	floor / middle / ceiling
III	300–1000	8	0.36–1.82	10/20/30	floor / middle / ceiling
IV	>1000	5	0.52–1.62	10/20/30	floor / middle / ceiling
Total	27–5429	44	0.36–2.06	10/20/30	floor / middle / ceiling

### 2.3. Definition of Indicators

To distinguish the spatially averaged fuel–air condition from the local flammability state, both the global equivalence ratio and local flammability indicators were defined. The global equivalence ratio  $\varphi$  was calculated from the total released HBNG volume, the HBR and the enclosed space volume. It represents the overall average fuel air condition in the enclosed space and was used only as a global reference parameter.

Natural gas was approximated as methane in the equivalence-ratio calculation. For a methane hydrogen mixture expressed in volume percentages, the equivalence ratio can be written as

$$\varphi = \frac{2C_{CH_4} + 0.5C_{H_2}}{20.95 - 0.2095(C_{CH_4} + C_{H_2})} \quad (1)$$

where  $C_{CH_4}$  and  $C_{H_2}$  are the volume percentages of methane and hydrogen. When globally averaged concentrations estimated from the released gas volume are used, Eq. 1 gives  $\varphi$ . When pre ignition concentrations measured at a local point are used, Eq. 1 gives the local equivalence ratio  $\varphi_{loc}$ .

For the non-uniform flammable cloud in the enclosed space, local combustion indicators were further defined based on the pre ignition methane and hydrogen concentrations measured at each point. The local total fuel concentration  $C_{fuel}$  was defined as:

$$C_{fuel} = C_{CH_4} + C_{H_2} \quad (2)$$

The local HBR was defined as:

$$HBR_{loc} = \frac{C_{H_2}}{C_{CH_4} + C_{H_2}} \quad (3)$$

According to the Le Chatelier mixing rule, the lower flammability indicator  $I_L$  and the upper flammability indicator  $I_U$  are introduced as local flammability criteria:

$$I_L = \frac{C_{CH_4}}{5} + \frac{C_{H_2}}{4} \quad (4)$$

$$I_U = \frac{C_{CH_4}}{15} + \frac{C_{H_2}}{75} \quad (5)$$

The Le Chatelier mixing rule was used here as an approximate local flammability screening criterion, rather than as a strict prediction of flame propagation in transient non-uniform clouds. When  $I_L \geq 1$  and  $I_U \leq 1$ , the mixture at the local measurement point was considered to be within the flammable range.

### 3. Results

#### 3.1. Flame Morphology

Figure 3 shows the flame evolution from 0 ms to 1250 ms after ignition for the four representative cases listed in Table 3. The flame morphology differs markedly among the cases. These cases were selected to illustrate typical differences in visible flame behavior and were not used alone to establish statistical trends.



**Figure 3.** Flame evolution for representative cases from 0 to 1250 ms.

**Table 3.** Representative cases for flame morphology comparison.

Case	HBR (vol%)	Released volume (SL)	Global equivalence ratio	Ignition delay time $t_d$ (s)	Ignition position	Flame visibility
a	10	368.5	0.96	30	floor	bright flame
b	10	366	0.96	674	floor	no visible flame

c	30	457.2	1	37	middle	bright flame weak
d	30	421.5	0.92	1459	middle	luminous spots

For Case a, the flame formed rapidly and intensified after ignition. By 750 ms, it had penetrated the membrane and expanded outward. Subsequently, a highly luminous orange-yellow flame appeared, indicating a relatively large visible flame region and strong flame luminosity under the short-delay condition. Case b had a HBR and global equivalence ratio similar to those of Case a, whereas the ignition delay time  $t_a$ , increased to 674 s. During the observation period, no sustained flame propagation was observed. Only a weak, localized blue flame appeared in the lower-left region at approximately 750 ms, indicating that the longer ignition delay markedly suppressed the development of the visible flame.

Case c exhibited the strongest visible flame development among the four representative cases. A relatively large flame region had already formed by 250 ms. After 500 ms, the flame penetrated the membrane and developed into a large-area, highly luminous bright-yellow flame. Its visible flame extent was significantly larger than that in Case a. Case d had the same HBR and a similar global equivalence ratio as Case c, but its ignition delay time  $t_a$ , increased to 1459 s. In this case, no strong outwardly expanding flame comparable to that in Case c was formed. Instead, several short-lived blue flames appeared in the upper-right region after rupture of the upper membrane at the later stage.

These qualitative observations show that ignition delay affected the apparent visible-flame development of the non-uniform HBNG cloud. Under short-delay conditions, brighter flames and wider visible propagation were observed. Under long-delay conditions, the visible flame became weaker or even difficult to observe, suggesting a reduction in the optically observable flame region. However, visible flame morphology should not be interpreted as a direct measure of total combustion intensity, because it is affected by local concentration distribution, flame position, hydrogen flame visibility, and optical observation conditions.

### 3.2. Concentration Field Evolution Under Long Ignition Delay Time

To help interpret the weakened visible flame development in Case d under the long ignition-delay condition, this case was selected to analyze the pre-ignition concentration evolution of the HBNG–air cloud. Based on the local parameters defined in Section 2.3, the variations in fuel concentration, fuel composition, and flammability state at different heights along the central axis were examined. This section focuses only on the vertical concentration field along the central axis, rather than reconstructing the full three-dimensional cloud.

Figure 4 shows the variations in methane and hydrogen concentrations during leakage and the subsequent ignition-delay period in Case d. The leakage duration was 31 s, and the ignition delay time  $t_a$  was 1459 s. During leakage, methane first accumulated near the bottom, reaching 26.5% at the bottom measurement point at 44 s. After leakage stopped, methane continued to migrate under buoyancy and diffusion. The top and middle measurement points reached their peak methane concentrations at approximately 204 s and 1440 s, respectively, indicating a transition from bottom enrichment to redistribution toward the middle and upper regions.

Hydrogen migrated faster than methane. The bottom, middle, and top measurement points reached their peak hydrogen concentrations at approximately 32 s, 60 s, and 88 s, respectively, reflecting the higher diffusivity and buoyant tendency of hydrogen. At ignition, the methane concentrations at the bottom, middle, and top were 5.17%, 4.38%, and 4.80%, respectively, indicating that methane had become nearly uniform. In contrast, hydrogen still showed vertical stratification. At ignition, the hydrogen concentration at the bottom approached the upper measurement range of the hydrogen sensor, whereas the measured values at the middle and top decreased to 2.94% and 2.05%, respectively. This representative case indicates that, under long ignition-delay conditions, the

HBNG cloud does not simply undergo uniform dilution. Instead, methane becomes nearly homogenized, whereas hydrogen remains vertically stratified.

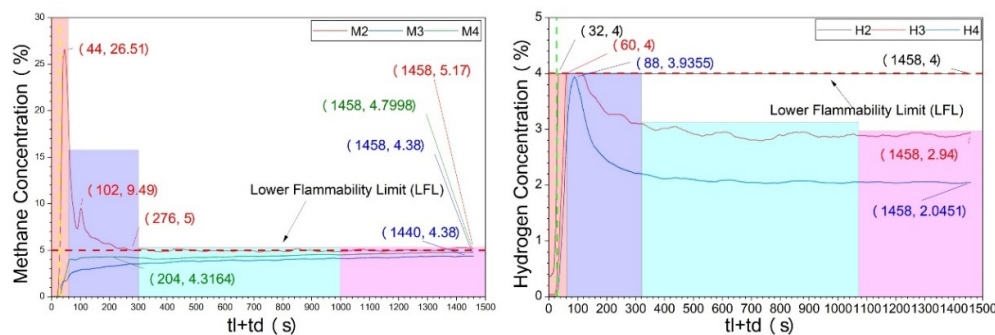


**Figure 4.** CH<sub>4</sub> and H<sub>2</sub> concentrations during the leakage and ignition delay periods in Case d.

Figure 5 shows the temporal evolution of  $C_{fuel}$ ,  $HBR_{loc}$ ,  $\phi_{loc}$ , and flammability indicators at different heights along the central axis.

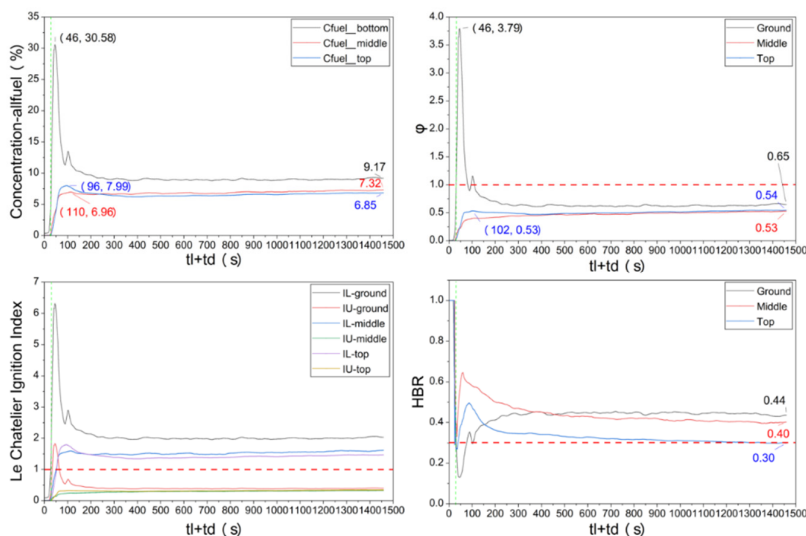


**Figure 5.** Temporal evolution of local flammability parameters along the central axis.

The local total fuel concentration indicates that the leaked gas first formed a high-concentration region near the bottom.  $C_{fuel}$  at the bottom reached 30.58% at approximately 46 s, much higher than those at the middle and top measurement points, which reached 7.99% at 96 s and 6.96% at 110 s, respectively. This suggests that the cloud initially accumulated near the bottom and then migrated toward the middle and upper regions. Therefore,  $C_{fuel}$  can characterize the local concentration of combustible fuel components, but it is insufficient to determine the local combustion behavior by itself.

In the early leakage stage,  $HBR_{loc}$  at all heights was higher than the HBR of the leakage source, indicating preferential hydrogen migration during soil seepage and entry into the confined space. With increasing time,  $HBR_{loc}$  gradually decreased and tended to stabilize, as subsequent methane migration and internal mixing weakened the early hydrogen-enrichment effect. Before ignition,  $HBR_{loc}$  remained different at the bottom, middle, and top measurement points, indicating persistent vertical non-uniformity in fuel composition.

The flammability indicators further show that although the bottom region had the highest  $C_{fuel}$  in the early stage, it did not correspond to the most favorable combustion state. Near the bottom peak,

$\varphi_{loc}$  reached 3.79, indicating an obviously fuel-rich mixture in this region. As the ignition delay time increased, the fuel concentration at the bottom gradually decreased, while the middle and upper regions gradually entered or approached the flammable range. Before ignition,  $C_{fuel}$  at the bottom, middle, and top was 9.17%, 7.32%, and 6.85%, respectively, with corresponding  $\varphi_{loc}$  values of 0.65, 0.53, and 0.54. Based on the local equivalence ratio and flammability indicators, the mixtures at all three heights were fuel-lean but still within the flammable range. In terms of temporal evolution,  $C_{fuel}$  and  $\varphi_{loc}$  varied almost synchronously. At the bottom, both reached their peaks at approximately 46 s, while the middle and top entered a relatively stable stage at similar times. This indicates that, under this operating condition, the local equivalence ratio mainly varied with the local fuel concentration, while  $HBR_{loc}$  primarily reflected the relative composition of methane and hydrogen.

A long ignition-delay period allowed continuous reconfiguration of the local fuel composition and flammability state. The global equivalence ratio or any single indicator cannot reliably predict the actual local combustion conditions in a non-uniform cloud; instead, the pre-ignition state should be evaluated based on the dynamic evolution of local concentration, fuel composition, and equivalence ratio.

### 3.3. Effect of Global Equivalence Ratio on Peak Temperature

Figure 6 shows the variation of  $T_{max}$  with the global equivalence ratio  $\varphi$  for the 44 experimental cases. The quadratic polynomial fit yielded a coefficient of determination  $R^2$  of only 0.026, indicating a very weak correlation between the two variables. Although the fitted curve showed a maximum near  $\varphi = 1.367$ , this trend has limited predictive significance because of the strong scatter in the experimental data.  $T_{max}$  ranged from 99.8 °C to 302.7 °C. These values represent point-measured thermal responses rather than flame temperatures. Even within the near-stoichiometric to moderately fuel-rich range of  $\varphi = 1.1$ – $1.367$ ,  $T_{max}$  varied from 131 °C to 268 °C, with a span of 137 °C. The case with the highest global equivalence ratio,  $\varphi = 2.06$ , was clearly fuel-rich, but its  $T_{max}$  was only 99.8 °C, the lowest value among all experiments. These results indicate that there is no monotonic relationship between the global equivalence ratio and the peak temperature at the central measurement point. Therefore, the global equivalence ratio alone was insufficient to predict the local point-measured thermal response of the non-uniform cloud.

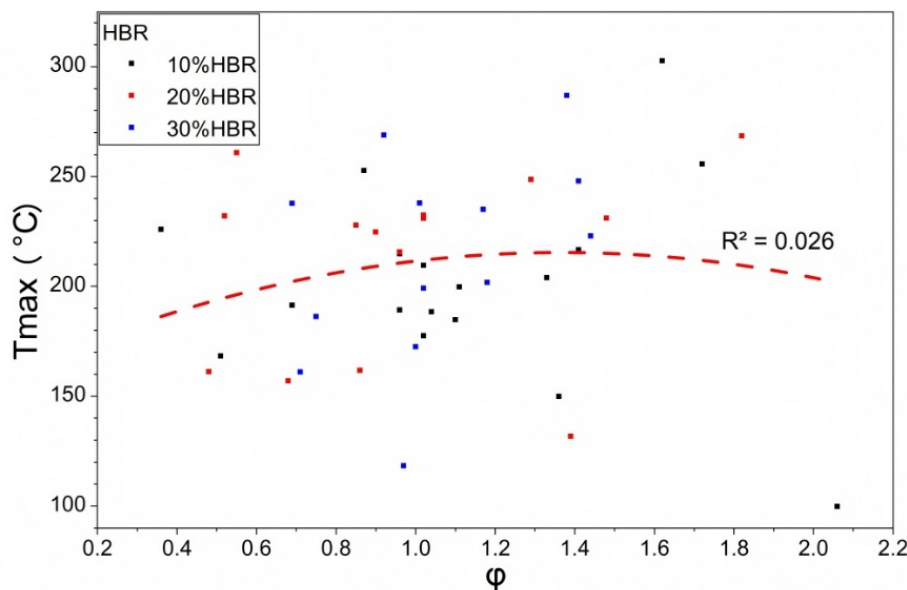
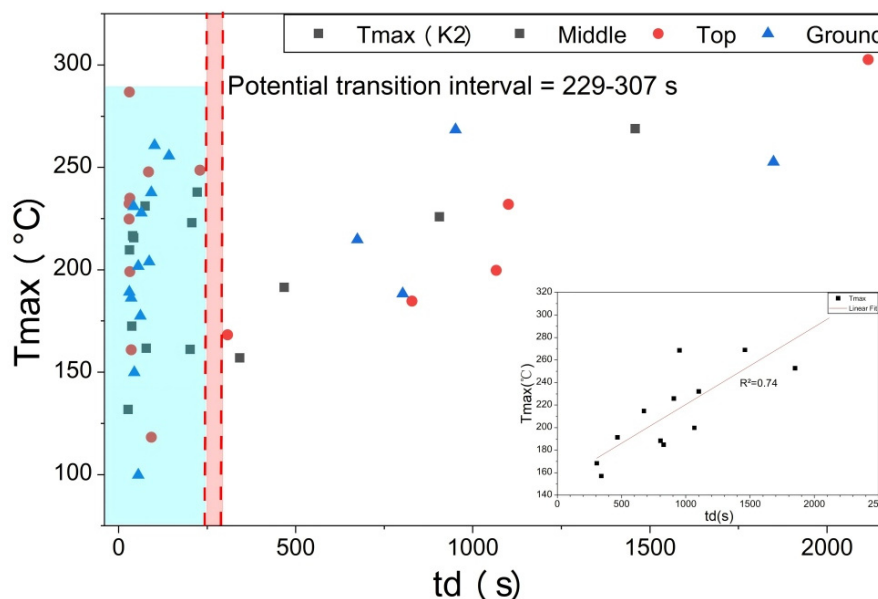


Figure 6. Effect of global equivalence ratio on peak temperature.

### 3.4. Effect of Ignition Delay Time on Peak Temperature

Figure 7 presents the relationship between  $t_d$  and  $T_{\max}$ , with different symbols representing ignition at the mid-height, top, and ground-level positions. The data show clear regime-dependent characteristics. In the short-delay region, mainly with  $t_d < 229$  s, the data points are densely distributed but highly scattered, and  $T_{\max}$  fluctuates over a wide range. This indicates that, under short ignition-delay conditions,  $T_{\max}$  is not governed by  $t_d$  alone, but is jointly affected by the local concentration distribution, ignition position, and transient disturbances.



**Figure 7.** Relationship between ignition delay time  $t_d$  and peak temperature  $T_{\max}$ .

For the subset with  $t_d > 307$  s,  $T_{\max}$  showed an increasing trend with  $t_d$  in the present dataset. Because no experimental data were available in the interval of 229–307 s, this interval was treated as a data gap separating the short-delay and long-delay subsets, rather than as a sharply defined physical transition threshold. The inset in Figure 7 shows the linear fitting result for the long-delay region. The corresponding  $R^2$  value of 0.74 indicates a relatively strong positive association between  $t_d$  and  $T_{\max}$  within this long-delay subset.

Table 4 shows that the goodness of fit improved markedly as the short-delay data were progressively excluded. The strong scatter in the short-delay region weakened the overall association, whereas the increasing trend of  $T_{\max}$  with  $t_d$  became more apparent after the short-delay data were excluded.

**Table 4.** Linear fitting results under different ignition-delay thresholds.

Lower threshold of ignition delay time	Sample size, n	Slope	$R^2$
$t_d > 142$ s	18	0.039	0.31
$t_d > 229$ s	15	0.047	0.42
$t_d > 307$ s	13	0.069	0.74

The above trend in  $T_{\max}$  is consistent with the concentration-field reconfiguration mechanism described in Section 3.2. During the long-delay period, buoyancy-driven fuel migration and redistribution from the lower region toward the middle and upper regions altered the local combustion conditions near the central measurement region. This compositional redistribution may

explain why the visible flame development weakened while the peak temperature at the central measurement point increased in the long-delay subset. Therefore, in the present soil-seepage experiments, long-delay ignition was associated with a higher point-measured thermal response in the middle region of the enclosure, indicating that local thermal hazard may not necessarily decrease after a prolonged ignition delay.

### 3.5. Effect of Ignition Delay Time on Time to Peak Temperature

Figure 8 shows the distribution of  $t_{\max}$  as a function of  $t_d$ . The 44 experimental cases were divided into four groups according to the ignition-delay ranges defined in Table 2. The median values of  $t_{\max}$  in the four groups were 3, 3.5, 5, and 5 s, respectively, showing only a slight increasing trend with increasing  $t_d$ . Although  $t_d$  increased from 27 s to 5429 s, spanning more than two orders of magnitude, the median of  $t_{\max}$  increased by only 2 s. The main bodies of the box plots for all groups were concentrated within 2–7 s, indicating that the thermal response time scale at K2 was similar under most operating conditions.

Three clear outliers were observed. The ground-level ignition case at  $\varphi = 2.06$  gave a  $t_{\max}$  of 24 s and was strongly fuel-rich. The top-ignition case at  $\varphi = 0.51$  reached a  $t_{\max}$  of 63 s and was strongly fuel-lean. The mid-height ignition case at  $\varphi = 0.36$  gave a  $t_{\max}$  of 10 s and was also strongly fuel-lean. All outliers occurred under conditions far from stoichiometry, indicating that the anomalous peak temperature times are more likely associated with extreme local mixing states rather than a direct effect of  $t_d$ .

Figure 9 shows the distribution of  $t_{\max}$  for different ignition positions. After excluding the aforementioned extreme outliers, the data for ground-level, mid-height, and top ignition largely overlap and converge within 2–7 s. The scatter points show neither a monotonic trend with  $t_d$  nor clear height-dependent stratification. Thus, after excluding the extreme equivalence-ratio outliers, no clear ignition-position-dependent stratification of  $t_{\max}$  was observed in the present dataset.

Together with the findings in Section 3.4, these results indicate that  $t_{\max}$  was more sensitive to ignition-delay-associated cloud redistribution, particularly in the long-delay subset, whereas  $t_{\max}$  remained on the order of a few seconds in most cases. This suggests that the ignition-delay period mainly affected the peak temperature level through local concentration-field reconfiguration, rather than altering the characteristic time scale of the local thermal response. As a result,  $t_{\max}$  remains on the order of a few seconds in most cases.

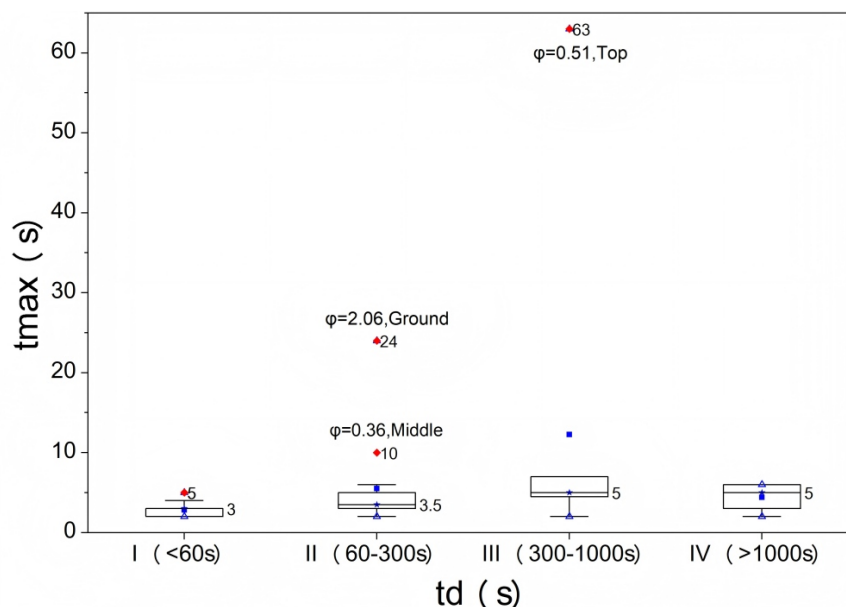


Figure 8. Distribution characteristics of delay time and time to peak temperature.

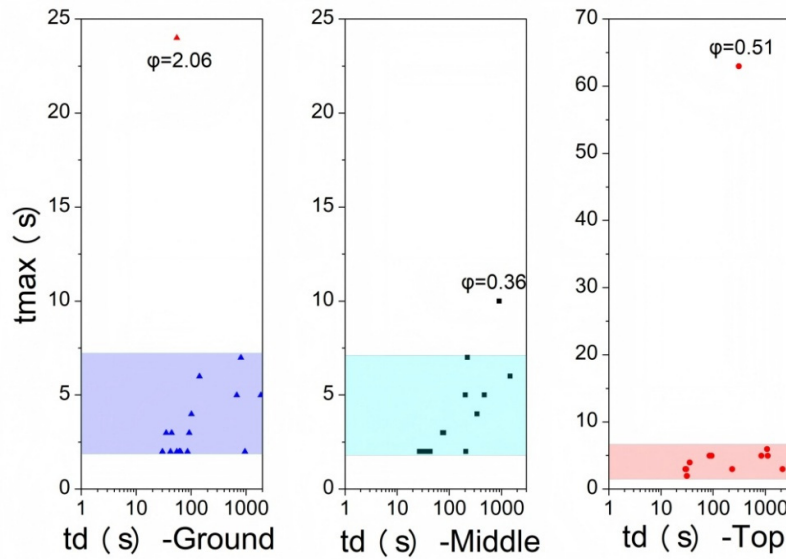


Figure 9. Distribution of time to peak temperature  $t_{max}$  for different ignition positions.

### 3.6. Vertical Spatial Distribution of Peak Temperature

Figure 10 shows the vertical distribution of peak temperature along the height direction of the enclosed space for six cases arranged on the central axis. For each HBR, two representative cases were selected. The corresponding case parameters and measured results are listed in Table 5.

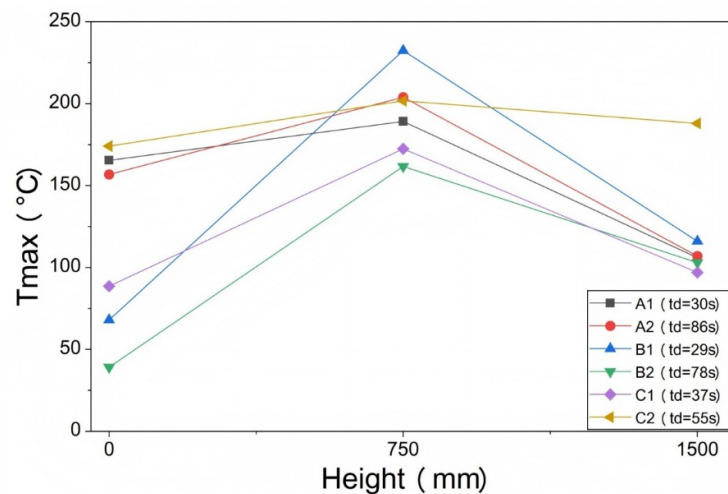


Figure 10. Vertical distribution of peak temperature.

Table 5. Experimental conditions and measured results for comparison of vertical temperature distributions.

Case	HBR (%)	$\varphi$	$t_d$ (s)	Ignition position	K1 $T_{max}$ (°C)	K1 $t_{max}$ (s)	K2 $T_{max}$ (°C)	K2 $t_{max}$ (s)	K3 $T_{max}$ (°C)	K3 $t_{max}$ (s)
A1	10	0.96	30	floor	165.4	2	189.2	2	106	2
A2	10	1.33	86	floor	156.8	1	204	2	107	2
B1	20	1.02	29	ceiling	68	3	232.4	3	116	3

B2	20	0.86	78	middle	39.2	4	161.7	3	103	4
C1	30	1	37	middle	88.6	2	172.5	2	97	2
C2	30	1.18	55	floor	174.1	2	201.8	2	188	2

All six cases exhibited a consistent pattern: the peak temperature at K2 was consistently higher than those at K1 and K3, indicating a vertical distribution characterized by higher values in the middle and lower values in the upper and lower regions. This result shows that, within the range of test conditions examined in this study, the central region of the enclosed space exhibited the strongest thermal response, suggesting that this region was more likely to correspond to relatively favorable local combustion conditions at the time of ignition. It should be noted that the peak-temperature distribution mainly reflects the post-combustion thermal response characteristics and cannot be used alone to reconstruct the complete concentration field.

Both A1 and A2 had a HBR of 10%, and both were ignited at the floor. Their  $t_d$  values were 30 s and 86 s, with global equivalence ratios of 0.96 and 1.33, respectively. Although their global equivalence ratios are not identical, their peak temperature distributions still show clear differences. Compared with A1, A2 exhibits a decrease in peak temperature at K1 from 165.4 °C to 156.8 °C, an increase at K2 from 189.2 °C to 204.0 °C, and little change at K3. This indicates that, between these two cases, the region with a strong thermal response became more pronounced from the lower region toward the center. This phenomenon is consistent with the trend of redistribution of combustible components from the lower region to the middle-to-upper region under long-delay conditions, as revealed in Section 3.2.

For Case C2, the peak temperatures at the three measurement points were 174.1 °C, 201.8 °C, and 188.0 °C, respectively, with a maximum difference of only 28 °C, which was significantly smaller than the range of 83 °C to 164 °C observed in the other cases. This indicates that the vertical thermal response in this case tended to be more uniform. One possible explanation is that the relatively high HBR of 30% promoted vertical diffusion and species exchange within the gas mixture, thereby reducing the vertical difference in peak temperature. However, this result may also have been jointly influenced by the ignition position and equivalence ratio.

Table 5 shows that, in each case, the differences in the times to peak temperature among K1, K2, and K3 were generally no more than 1 s, indicating that the thermal response time scales at different heights were similar. Nevertheless, the peak temperatures at the three heights still showed significant differences, further confirming that the vertical distribution of peak temperature was mainly governed by the local pre-ignition combustible conditions and heat release intensity, rather than by differences in the thermal response time scale.

## 4. Discussion

### 4.1. Comparison with the Study by Yang et al.

Yang et al. [21] investigated the non-uniform combustion and explosion characteristics of pure hydrogen leakage clouds in a small-scale horizontal pipe open at both ends, with ignition delay times ranging from 0 to 1200 ms. They found that, as the ignition delay time increased, leakage-induced turbulence decayed while buoyancy-driven stratification intensified. As a result, the maximum flame speed and overpressure generally decreased, and 800 ms was identified as the critical point for the transition from turbulence-dominated to buoyancy-dominated behavior.

In the present study, the visible flame also weakened with increasing delay time, whereas the peak temperature at K2 increased in the long-delay regime. This difference can be attributed to the distinct fluid-dynamic mechanisms and boundary conditions of the two scenarios. The study by Yang et al. focused on the short-time diffusion of a pure hydrogen momentum jet in a pipe with open boundaries, where unburned gas could continuously escape through the open ends. The delay-induced concentration attenuation was therefore monotonic and irreversible, and the combustion

intensity decreased monotonically accordingly. In the present study, however, after HBNG seeped through the porous soil medium and entered the enclosed space, the gas was retained inside the space and could not escape. The delay stage was not simply a process of concentration attenuation, but rather involved the dynamic reconstruction of the concentration field under long-duration, multicomponent, closed-boundary conditions over 27–5429 s, during which CH<sub>4</sub> and H<sub>2</sub> continuously migrated at different rates under buoyancy. This reconstruction process could gradually improve the local combustible conditions in the central region with increasing delay time, leading to the coexistence of weakened overall visible flame behavior and enhanced local thermal hazard.

Therefore, the conclusion drawn by Yang et al. that increasing ignition delay time leads to decreases in flame speed and overpressure is mainly applicable to the early-stage leakage and diffusion process of pure hydrogen in open, small-scale pipes. Consequently, this conclusion should be applied with caution when considering non-uniform HBNG clouds induced by soil seepage in enclosed spaces.

#### 4.2. Discrepancy Between Macroscopic Flame and Local Thermal Response

The discrepancy between visible flame morphology and local thermal response indicates that qualitative flame appearance alone cannot be used to evaluate combustion intensity in a non-uniform HBNG cloud. The visible flame mainly reflects the optically observable combustion region, whereas the thermocouple signal reflects the local point-measured thermal response near a fixed position. Therefore, a weaker visible flame does not necessarily indicate a lower local point-measured thermal response.

The times to peak temperature further support this mechanism. In most cases, the times to peak temperature remained on the order of several seconds and did not vary significantly with  $t_a$ , indicating that the delay process altered the local heat release intensity rather than the intrinsic time scale of combustion dynamics. Therefore, the macroscopic appearance of the visible flame cannot replace local temperature measurements when assessing the thermal exposure associated with a non-uniform cloud.

#### 4.3. Limitations of the Global Equivalence Ratio

The global equivalence ratio can only represent the spatially averaged fuel–air ratio based on the total leaked amount, and cannot reflect the internal concentration gradients or local combustible states within a non-uniform cloud. The experimental results show that cases with similar global equivalence ratios can exhibit different flame morphologies and thermal responses. The concentration analysis of the long-ignition-delay experiments also shows that, before ignition, the methane concentration, hydrogen concentration, local HBR, and local equivalence ratio differed at different heights. The coefficient of determination,  $R^2$ , for the fit between  $T_{\max}$  and  $\varphi$  was only 0.026, indicating that there was almost no correlation between them.

For non-uniform clouds induced by soil seepage, the assessment of local thermal hazard must jointly consider multidimensional flammability indicators, such as the local total fuel concentration, local HBR, and local equivalence ratio. The global equivalence ratio cannot be used alone as a reliable predictor of local point-measured thermal response in such non-uniform clouds.

#### 4.4. Engineering Implications

The above results have direct implications for accident risk management in buried HBNG pipeline networks. In enclosed spaces such as underground utility tunnels and valve chambers, an increase in the waiting time after leakage cessation may reduce outward visible-flame development, but it does not necessarily reduce the local thermal exposure in the central region because of buoyancy-driven redistribution of fuel components. Therefore, risk assessment for such scenarios should not determine safety solely based on the waiting time after leakage or the global equivalence

ratio. Instead, the dynamic evolution of the local pre-ignition concentration field and local combustibility should be incorporated as core evaluation elements. Existing safety criteria based on assumptions of homogeneous premixing or global parameters should be applied with caution when used for non-uniform leakage scenarios induced by soil seepage.

#### 4.5. Experimental Limitations and Boundary Conditions

Owing to the large-scale and soil-seepage-dependent nature of the experiments, exact repetition of each operating condition was difficult because small variations in soil packing, seepage pathways, and cloud redistribution could not be fully eliminated. Therefore, the conclusions of this study should be interpreted as trend-based evidence from 44 valid experimental cases rather than as deterministic predictions for individual leakage scenarios.

During the ignition-delay period, the enclosure had no designed ventilation opening and was treated as a quasi-closed space. The observed PE-film inflation before rupture after ignition indicates that gas was retained before ignition. Therefore, the long-delay stage was mainly interpreted as a quasi-closed redistribution process of CH<sub>4</sub> and H<sub>2</sub> rather than a ventilation-controlled dilution process.

The measured peak temperatures represent local point-measured thermal responses rather than flame temperatures or the maximum temperature of the entire cloud. The thermocouples recorded transient gas temperatures at fixed positions, and the flame front did not necessarily pass directly through each junction. Heat losses, thermocouple response time, PE-film rupture, and post-rupture air entrainment may also have reduced the measured temperature. Therefore,  $T_{\max}$  should not be compared directly with the adiabatic flame temperature of HBNG–air mixtures. In this study,  $T_{\max}$  is used only to compare local thermal exposure under different ignition-delay conditions. Future studies should combine denser concentration measurements, pressure sensors, and full-field temperature diagnostics to further clarify the coupling between cloud redistribution, flame propagation, and thermal response. Because pressure was not measured in the present study, the results should not be used to infer overpressure or explosion severity.

The nominal electrical ignition energy was calculated from the recorded discharge power and ignition duration. However, the effective energy deposited into the combustible mixture was not directly measured. Therefore, ignition energy was treated as a documented ignition condition rather than as an independently controlled variable.

In addition, the HBR, global equivalence ratio, ignition position, released volume, and ignition delay time were not fully orthogonalized. Therefore, the observed relationship between ignition delay and peak temperature should be interpreted as a coupled trend associated with post-leakage cloud redistribution, rather than as the isolated effect of ignition delay alone.

## 5. Conclusions

Based on 44 experiments on HBNG leakage through soil into an enclosed space, this study investigated the association between ignition delay, flame behavior, and local point-measured thermal response of non-uniform HBNG clouds. The main conclusions are as follows.

1. The ignition-delay period was associated with changes in qualitative visible-flame morphology. Under short-delay conditions, brighter flames and wider visible propagation were observed. Under long-delay conditions, the visible flame became weaker or was barely visible. These observations indicate a reduction in apparent visible-flame development, but they should not be interpreted as a direct quantitative measure of combustion intensity.

2. Long ignition-delay periods allowed substantial reconstruction of the local pre-ignition concentration field. Hydrogen preferentially migrated because of its higher diffusivity and buoyant rise behavior, whereas methane was redistributed from the bottom toward the middle-to-upper regions over a longer time scale. Under long-delay conditions, a near-uniform methane distribution coexisted with vertical hydrogen stratification. Before ignition, the local total fuel concentration, local HBR, local equivalence ratio, and combustibility indicators still differed at different heights.

3. The local peak temperature and qualitative visible-flame morphology did not vary synchronously. In the short-delay regime,  $T_{\max}$  exhibited strong scatter. For the long-delay subset with  $t_d > 307$  s, the peak temperature at K2 showed a positive association with ignition delay in the present dataset, with  $R^2 = 0.74$ . This trend suggests that post-leakage cloud redistribution may improve the local combustible condition near the central region. In contrast,  $t_{\max}$  was mostly concentrated within 2–7 s and showed little dependence on  $t_d$ , indicating that the ignition-delay period mainly changed the peak level rather than the response time scale of the local thermal response. For the six selected central-axis cases, K2 recorded higher peak temperatures than K1 and K3, suggesting a stronger point-measured thermal response in the central region under these selected conditions.

4. Unlike the monotonic decay of combustion intensity with diffusion time reported for open-boundary, short-duration pure-hydrogen leakage scenarios, prolonged ignition delay in enclosed soil-seepage scenarios does not necessarily reduce the local point-measured thermal response. No monotonic relationship was observed between the global equivalence ratio and the peak temperature at K2, with  $R^2 = 0.026$ . This indicates that the global equivalence ratio alone is insufficient for predicting local thermal response in non-uniform HBNG clouds. Accident risk assessment should therefore consider the dynamic evolution of the local pre-ignition concentration field and local combustibility, rather than relying solely on waiting time after leakage cessation or global equivalence ratio.

**Author Contributions:** Conceptualization, Wenxin.Guo; methodology, Shaohua.Dong; data curation, Wenxin.Guo.; writing—original draft preparation, Wenxin.Guo; writing—review and editing, Jiamei.Li; supervision, Shaohua.Dong.; project administration, Haotian.Wei.; funding acquisition, Shaohua.Dong. All authors have read and agreed to the published version of the manuscript.

**Funding:** This research was funded by the Beijing Association for Science and Technology through the project “Strategic Study on the Safety of Hydrogen Energy Production, Storage, Transportation, and Utilization in Beijing”, grant number ZX20230307.

**Institutional Review Board Statement:** Not applicable.

**Informed Consent Statement:** Not applicable.

**Data Availability Statement:** The raw data supporting the conclusions of this article will be made available by the authors on request.

**Acknowledgments:** During the preparation of this manuscript, the authors used ChatGPT for English language polishing. The authors reviewed and edited the output and take full responsibility for the content of this publication.

**Conflicts of Interest:** The authors declare no conflicts of interest.

## References

1. Zacepins, A.; Kotovs, D.; Komasilovs, V.; Kvisis, A. Economic Modelling of Mixing Hydrogen with Natural Gas. *Processes* 2024, 12, 262.
2. Zheng, Z.; Xiwang, A.; Sun, Y. Optimal Scheduling of Integrated Energy System Considering Hydrogen Blending Gas and Demand Response. *Energies* 2024, 17, 1902.
3. Fetisov, V. Analysis of numerical modeling of steady-state modes of methane–hydrogen mixture transportation through a compressor station to reduce CO2 emissions. *Sci. Rep.* 2024, 14, 10605.
4. Xue, Y.; Li, X.; Liu, Y.; Yuan, J.; Hua, J.; Wu, Y. Adaptability Study of Pressure Regulators in Hydrogen-Blended Natural Gas Pipelines. *ACS Omega* 2025, 10, 50415-50430.
5. Martin, P.; Ocko, I.; Esquivel-Elizondo, S.; Kupers, R.; Cebon, D.; Baxter, T.; Hamburg, S. A review of challenges with using the natural gas system for hydrogen. *Energy Sci. Eng.* 2024, 12, 3995-4009.

6. Raj, A.; Larsson, I.A.S.; Ljung, A.-L.; Forslund, T.; Andersson, R.; Sundström, J.; Lundström, T.S. Evaluating hydrogen gas transport in pipelines: Current state of numerical and experimental methodologies. *Int. J. Hydrogen Energy* 2024, 67, 136-149.
7. Massarweh, O.; Bicer, Y.; Abushaikha, A. Technoeconomic analysis of hydrogen versus natural gas considering safety hazards and energy efficiency indicators. *Sci. Rep.* 2025, 15, 29601.
8. Li, M.; Wang, Z.; Jiang, J.; Lin, W.; Ni, L.; Pan, Y.; Wang, G. Numerical Simulation and Consequence Analysis of Full-Scale Jet Fires for Pipelines Transporting Pure Hydrogen or Hydrogen Blended with Natural Gas. *Fire* 2024, 7, 180.
9. Ban, J.; Wang, X.; Zhou, L.; Yang, W.; Hu, J.; Liu, T.; Liu, G. The Effect of Heterogeneous Backfill Soil on Leakage Behavior of Hydrogen-Blended Natural Gas Pipelines. *ACS Omega* 2026, 11, 8807-8825.
10. Wang, X.; Hou, T.; Ba, X.; Tan, Y. Simulation of Diffusion Characteristics and Risk Analysis of Natural Gas in an Underground Enclosed space: A Case Study. *ACS Omega* 2025, 10, 18910-18923.
11. Gong, X.; Li, H.; Li, C.; Kou, M.; Kong, L.; Liu, H. Research on leakage and diffusion behavior of hydrogen doped natural gas in integrated pipeline corridors based on data drive. *Sci. Rep.* 2025, 15.
12. Chang, W.; Wang, W.; Guo, Y.; Wang, L.; Li, Z. Diffusion characterization of hydrogen-blended natural gas leakage for buried pipeline based on simulation. *Int. J. Hydrogen Energy* 2025.
13. Chen, S.; Li, M.; Dong, H.; Meng, L.; Guan, B.; Zhou, S.; Wang, S.; Niu, C. Numerical investigation for hazardous gas cloud form and dissipation behaviour of hydrogen-blended natural gas in a enclosed space. *R. Soc. Open Sci.* 2025, 12.
14. Tian, Y.; Tian, T.; Ren, G.; Zhang, J. Numerical simulation of hydrogen mixing process in T-junction natural gas pipeline. *Materials* 2025, 18.
15. Wang, Y.; Xu, C.; Zhao, G.; Zeng, Y.; Han, R.; He, T. Numerical simulation study on hydrogen leakage and explosion of hydrogen fuel cell buses. *Sci. Rep.* 2025, 15.
16. Nosek, R.; Patsch, M.; Pilát, P.; Zvada, B.; Backa, A. Flashback behavior and safety implications of hydrogen–natural gas mixtures. *Sci. Rep.* 2025, 15.
17. Li, M.; Chen, S.; Jiang, W.; Li, Y.; Xu, Z.; Guan, B.; Wang, X.; Lin, X.; Liu, T. Numerical simulation analysis of the hydrogen-blended natural gas leakage and ventilation processes in a domestic house. *ACS Omega* 2023, 8, 34610-34628.
18. Amer, M.; Hoseyni, S.M.; Cordiner, J. Fuelling the future with safe hydrogen transportation through natural gas pipelines: A quantitative risk assessment approach. *Trans. Indian Natl. Acad. Eng.* 2024, 9, 763-781.
19. Deng, B.; Huang, X.; Lyu, S.; Aimaieraili, D. Numerical Investigation on the Diffusion and Ventilation Characteristics of Hydrogen-Blended Natural Gas Leakage in Indoor Spaces. *Buildings* 2025, 15(21), 3833.
20. Liu, Q.; Liu, Z.; Peng, S.; Liu, C.; Liu, C.; Liu, L.; Zhou, R.; Zhi, S.; Fan, T.; Li, P. Effects of Hydrogen Blending Ratio and Equivalence Ratio on the Dynamic Characteristics of Deflagration Shock Waves of CH<sub>4</sub>/H<sub>2</sub> Mixtures. *ACS Omega* 2024, 9, 23853-23863.
21. Yang, W.; Zhang, K.; Jiang, B.; Yang, X.; Zhang, Y. Experimental study on the effect of diffusion time on non-uniform hydrogen explosion induced by leakage. *Int. J. Hydrogen Energy* 2025, 177, 151614.

**Disclaimer/Publisher's Note:** The statements, opinions and data contained in all publications are solely those of the individual author(s) and contributor(s) and not of MDPI and/or the editor(s). MDPI and/or the editor(s) disclaim responsibility for any injury to people or property resulting from any ideas, methods, instructions or products referred to in the content.